Eliminating backwall effects in the phased array imaging of near backwall defects

Chao Zhang,[1, a)] Peter Huthwaite,[1] and Michael Lowe[1]

Department of Mechanical Engineering, Imperial College London,

Exhibition Road, South Kensington, London SW7 2AZ,

United Kingdom

Ultrasonic array imaging is widely used to provide high quality defect detection and characterization. However, the current imaging techniques are poor at detecting and characterizing defects near a surface facing the array, as the signal scattered from the defect and the strong reflection from the planar backwall will overlap in both time and frequency domains, masking the presence of the defect. To address this problem, this paper explores imaging algorithms and relevant methods to eliminate the strong artefacts caused by the backwall reflection. The Half-skip Total Focusing Method (HSTFM), the Factorization Method (FM) and the Time Domain Sampling Method (TDSM) are chosen as the imaging algorithms used in this paper. Then, three methods, referred to as FMC (Full Matrix Capture) subtraction, weighting function filtering and the truncation method, are developed to eliminate or filter the effects caused by the strong backwall reflection. These methods can be applied easily with few tuning parameters or little prior knowledge. The performances of the proposed imaging techniques are validated in both simulation and experiments, and the results show the effectiveness of the developed methods to eliminate the artefacts caused by the backwall reflections when imaging near backwall defects.

[a] chao.zhang13@imperial.ac.uk; Readers who are interested in accessing data associated with this paper are referred to www.imperial.ac.uk/non-destructive-evaluation where either the data or details of how to obtain the data can be found.

I. INTRODUCTION

The assessment of the size and type of fatigue cracks and stress corrosion cracks has long been a significant task for non-destructive evaluation. These cracks are commonly found near inaccessible interior surfaces, referred to here as 'backwalls', and are important to detect and characterise in safety-critical components under severe working environment (high pressure or high temperature) or cyclic loading, for example nozzles, piping components and vessel welds (Collins, 1993). Recently, the use of ultrasonic phased arrays to evaluate near backwall defects has attracted a lot of attention (Felice *et al.*, 2014, 2015; Iakovleva *et al.*, 2014; Zhang *et al.*, 2016). A great advantage of using ultrasonic phased arrays is that this allows the acquisition of Full Matrix Capture (FMC (Holmes *et al.*, 2005)) data. The FMC data contains a set of signals for all send-receive combinations in the array, giving a complete data set. The FMC data is achieved by using each element as a source transducer to excite ultrasound waves in turn, which is then measured by all of the elements in the array. After the acquisition of the FMC data, various post-processing algorithms, especially imaging algorithms, can be applied to the FMC data to image the defects under detection. Thus, phased array imaging provides a very convenient way to assess the defect, as the size and type of the defect can be measured and judged directly from the generated images. Recently, as a response to the challenge of characterising the defect (e.g. crack length and orientation) accurately from the image, a scattering matrix based approach (Bai *et al.*, 2015; Zhang *et al.*, 2010), which compares an experimentally acquired scattering matrix to a database of pre-calculated scattering matrices to characterize the defect, has been developed. This method has achieved a good accuracy based on the experiment array data, however, for this method, even for a limited type of defect, a large number of scattering matrices have to be calculated.

With the development and application of inverse scattering theory and computing technology, the imaging algorithms developed for phased array imaging have advanced significantly in recent years. Among all the existing imaging algorithms, the Beamforming methods are most common and are able to provide a direct image of the defect under detection. Typical examples include the Total Focusing Method (TFM) (Holmes *et al.*, 2005), the Synthetic Aperture Focusing Technique (SAFT) (Martin-Arguedas *et al.*, 2012) and inverse wave-field extrapolation (Portzgen *et al.*, 2007). These algorithms have been shown to provide reliable imaging of the defect but their resolution is diffraction limited, i.e. the highest resolution is half a wavelength (Fan *et al.*, 2014). In the last twenty years, super resolution algorithms, also called the sampling methods, which break this $\frac{\lambda}{2}$ limit, have been demonstrated and have received a lot of attention. Notable super resolution algorithms are the Linear Sampling Method (LSM) (Cakoni and Colton, 2003), the Factorization Method (FM) (Kirsch and Grinberg, 2008) and the Time-Reversal Multiple Signal Classification (TR-MUSIC) (Gruber *et al.*, 2004). Based on the experiment performed in (Simonetti, 2006), it has been proved that these methods have the ability to provide super resolution imaging of scatterers relevant to NDE beyond the diffraction limit. In addition to these algorithms, recently, a novel type of imaging algorithm called the direct sampling method has been proposed for shape reconstruction in inverse scattering problems, e.g. Time Domain Sampling Method (TDSM) (Guo *et al.*, 2016a), Orthogonality Sampling (Potthast, 2010) and Direct Sampling method (Ito *et al.*, 2012). All the imaging algorithms mentioned here are able to reconstruct the shape of a scatterer inside a component without prior knowledge of the geometry of the component or the physical properties of the scatterer.

Usually when inspecting such defects, the array has to be placed on the frontwall to conduct through-wall detection of the defect near the backwall. In these cases, the presence of the backwall brings a strongly reflecting planar interface which will introduce a strong specular reflection into the FMC data. As a result, for a typical FMC data set, the signal from the defect and the backwall reflection always overlaps in both time and frequency domain, thus, they are hard to separate via the existing signal processing techniques, for example deconvolution techniques (Cicero *et al.*, 2009). The presence of the strong backwall reflection will introduce strong artefacts that makes imaging of the defect difficult; these will be referred to as backwall effects throughout this paper. In response to this problem, J. Zhang et al. (Zhang *et al.*, 2016) have developed a method which separates the reference backwall reflection from non-overlapping signals and then propagates the reference backwall reflection to create a backwall reflection for overlapping signals. After that, the extraction of the defect signal can be achieved by a simple subtraction. The implementation of this method needs a prior TFM image to achieve the knowledge of the defect location and backwall location, and in order to minimise the error, the array should be aligned with the defect as much as possible. These prerequisites may limit the application of this method in real applications. E. Iakovleva et al. (Iakovleva *et al.*, 2014) also have developed the Echo Transformation Method (ETM) to allow the prediction and filtering of the backwall effects in the TFM images. However, this technique needs to analyse the propagation models of the longitudinal wave in order to recognise and predict the performance of the backwall reflection in the transverse mode TFM image, or the other way around. Recently, C. Zhang et al. (Zhang *et al.*, 2018) have developed a method, called the FMC subtraction, to suppress the backwall effects for the Factorization method imaging of near backwall defects.

In this paper, various approaches are evaluated. FMC subtraction is applied to some recently developed imaging algorithms (e.g. the Time Domain Sampling Method) to suppress the backwall effects when imaging near backwall defects. Other techniques which allow convenient elimination of backwall effects are then presented and their performance are compared with the FMC subtraction.

The rest of the paper is organised as follows. Firstly, in Section 2, we summarize the background theory about the forward and inverse scattering. The three imaging algorithms used in this paper, the HSTFM, the FM and the TDSM, are also introduced in this section. Then, a detailed introduction to the developed methods which eliminate the backwall effects caused by the backwall reflection is provided in Section 3. In this section, we also examine the effectiveness of the developed methods using simulation data. In Section 4, the performance of the imaging algorithms together with the backwall elimination methods are analysed through experiments.

II. BACKGROUND THEORY

In this section, we shall briefly review the background theory about the forward and inverse scattering problems considered in this paper. The formulation here is based on 2D acoustic scattering theory (Kinsler *et al.*, 2000). For the sake of simplicity, we will restrict our attention to the scattering problem of acoustic waves in an unbounded homogeneous

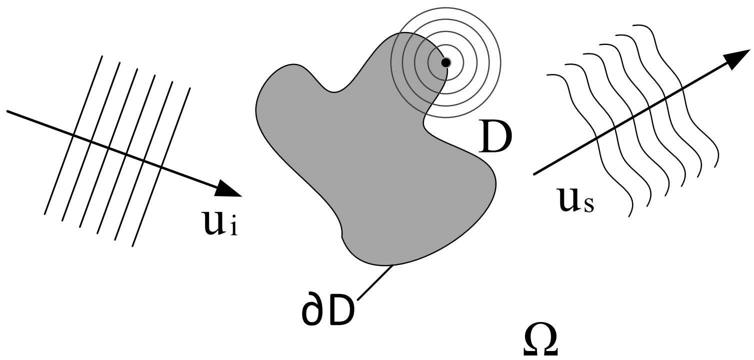

FIG. 1. Schematic of the 2D scattering problem. The bounded scatterer D is embedded in free space and the domain Ω is the exterior space to D. The scattered field measured by the array can only have been generated at the boundary of the scatterer but cannot have originated at any point outside the scatterer.

background space $\mathbb{R}^2$ that contains an impenetrable scatterer D with the Dirichlet (sound-soft) boundary condition, as shown in Fig. 1.

A. Problem setting

In order to give a basic understanding of the imaging algorithms which will be introduced in the following section, a comprehensive overview of the expansion of the forward and inverse scattering problem is given here. Our discussion here is also based on the problem set out in Fig. 1. We denote an incident plane wave by

$$U^i(\boldsymbol{x}, k; \boldsymbol{\theta}) = e^{ik(\boldsymbol{x}\cdot\boldsymbol{\theta})} \quad \boldsymbol{x} \in \mathbb{R}^2,\ \boldsymbol{\theta} \in \mathbb{S}^1, \tag{1}$$

where $\mathbb{S}^1$ denotes a unit circle in $\mathbb{R}^2$ and k is the wave number, which is actually the spatial frequency of a wave. The scattered field is denoted by U^s and the total field is denoted as

U. Then, we can have

$$U^s(\cdot,\cdot;\theta) = U - U^i(\cdot,\cdot;\theta), \quad \text{in } \mathbb{R}^2, \tag{2}$$

The forward obstacle scattering problem is to find a total field which satisfies the Helmholtz equation

$$\Delta U + k^2 U = 0 \quad \text{in } \mathbb{R}^2 \setminus \overline{D}. \tag{3}$$

Meanwhile, it is also necessary to satisfy the Sommerfeld radiation condition and the Dirichlet boundary condition, which are

$$\lim_{r\to\infty} \sqrt{r}\left(\frac{\partial U^s}{\partial r} - ikU^s\right) = 0, \quad \text{for } r = |\boldsymbol{x}|, \tag{4}$$

$$U^i + U^s = 0, \quad \text{on } \partial D \times \mathbb{R}^+, \tag{5}$$

According to (Colton and Kress, 2013), there exists a unique solution for Eqs. (3)-(5). Eq. (4) implies that the scattered field u^s has an asymptotic expansion

$$U^s(\boldsymbol{x},k;\boldsymbol{\theta}) = \frac{e^{ik|\boldsymbol{x}|}}{\sqrt{|\boldsymbol{x}|}} U_\infty(\hat{\boldsymbol{x}},k;\boldsymbol{\theta}) + \mathcal{O}(|\boldsymbol{x}|^{-\frac{3}{2}}) \tag{6}$$

as $|\boldsymbol{x}| \to \infty$ for all $(\boldsymbol{\theta},\hat{\boldsymbol{x}}) \in \mathbb{S}^1 \times \mathbb{S}^1$, where $\hat{\boldsymbol{x}} := \boldsymbol{x}/|\boldsymbol{x}|$. According to (Griesmaier, 2011), the representation of the so-called far field pattern u^∞ is given by

$$U^\infty(\hat{\boldsymbol{x}},k;\boldsymbol{\theta}) = \frac{e^{i\pi/4}}{\sqrt{8\pi k}} \int_{\partial D} \left(U^s(\boldsymbol{y},k;\boldsymbol{\theta}) \frac{\partial e^{-ik\hat{\boldsymbol{x}}\cdot\boldsymbol{y}}}{\partial v(\boldsymbol{y})} - \frac{\partial U^s(\boldsymbol{y},k;\boldsymbol{\theta})}{\partial v(\boldsymbol{y})} e^{-ik\hat{\boldsymbol{x}}\cdot\boldsymbol{y}}\right) ds(\boldsymbol{y}) \tag{7}$$

where $v(\boldsymbol{y})$ is the unit normal vector at $\boldsymbol{y} \in \partial D$. Solving Eqs. (3)-(5) is a well-posed problem (Pike and Sabatier, 2002) and several corresponding numerical methods for solving the forward problem can be found in (Chen *et al.*, 2017; Graham *et al.*, 2013).

In this paper, the inverse problem, which is also called the imaging problem, aims to reconstruct the location and shape of the scatterer D given the incident field U^i and the measurements of the far field pattern U^∞

$$\{U^\infty(\hat{\boldsymbol{x}}, k; \boldsymbol{\theta}) | \hat{\boldsymbol{x}} \in \Gamma, \quad \boldsymbol{\theta} \in \Gamma, \quad k = k_1, \cdots, k_M\}. \tag{8}$$

where $M : M \in \mathbb{N}$ is the number of wave numbers considered in the problem and Γ denotes some subset of $\mathbb{S}^1$. The far-field pattern is assumed to be illuminated from limited directions and measured at limited directions, i.e. we are concerned with limited-view scattered data (Kirsch and Grinberg, 2008). We refer to (Kirsch, 1996; Kirsch and Grinberg, 2008) for a more detailed derivation of the formulations for the forward and inverse scattering problems. The fundamental difference between the forward and the inverse problems is that the inverse problem is an ill-posed problem, and we refer to (Kirsch, 1996) for a more detailed explanation about the well-posedness and ill-posedness of these problems.

B. Imaging algorithms

In what follows, the imaging algorithm means the post processing method applied to the data obtained though Full Matrix Capture (FMC) (Holmes *et al.*, 2005) which is a data acquisition method designed for phased arrays. Phased array imaging implies that only limited aperture data is available (Kirsch and Grinberg, 2008). By assuming that FMC data is acquired, the knowledge of the time domain scattered data u^S or the relevant far-field pattern U^∞ in Eq. (8) is already known.

1. *Half-Skip Total Focusing Method*

The Half-Skip Total Focusing Method (HSTFM) is a modified Total Focusing Method (TFM) developed for imaging and sizing near backwall defects (Felice *et al.*, 2014). A comprehensive overview of TFM is given at first to help the understanding of HSTFM.

TFM is implemented by focusing a sound beam to each point in the region of interest and recording the reflections from these points. According to (Holmes *et al.*, 2005), based on the imaging setup shown in Fig. 2(a), the indicator function of TFM is given by

$$I_{TFM}(\boldsymbol{z}) = \int_{\Gamma_i}\int_{\Gamma_i} u^S(\boldsymbol{x_r}, \frac{|\boldsymbol{x_r}-\boldsymbol{z}|+|\boldsymbol{x_t}-\boldsymbol{z}|}{c_0}; \boldsymbol{x_t}) ds(\boldsymbol{x_r}) ds(\boldsymbol{x_t}). \tag{9}$$

where Γ_i is the surface where transmitters and receivers are located, $\boldsymbol{x_t} \in \Gamma_i$ is the location of the transmitter, $\boldsymbol{x_r} \in \Gamma_i$ is the location of the receiver and $u^S(\boldsymbol{x_r}, t; \boldsymbol{x_t})$ denotes the time domain scattered data from a transmitter located at $\boldsymbol{x_t}$ to a receiver located at $\boldsymbol{x_r}$. The ray path considered in TFM is the direct ray path, which is the wave that directly travels from the transmitter to the image point P and back to the receiver, as shown in Fig. 2(a). However, in the case of detecting a near backwall defect, there is additional complexity from the wave reflecting from the backwall, which is not accounted for in TFM. In response, Felice et al. (Felice *et al.*, 2015) developed the Half-Skip Total Focusing Method (HSTFM) to image and size the near backwall defects. Unlike TFM, HSTFM considers the 'half-skip' ray paths which are reflected on the backwall once, either before or after interacting with the defect, as shown in Fig. 2(b).

Imagine that there is a mirrored imaging point P_m located at $\boldsymbol{z_m}$, as shown in Fig. 2(c). The length of the post-defect reflection half-skip path defined in Fig. 2(b) is that of a path

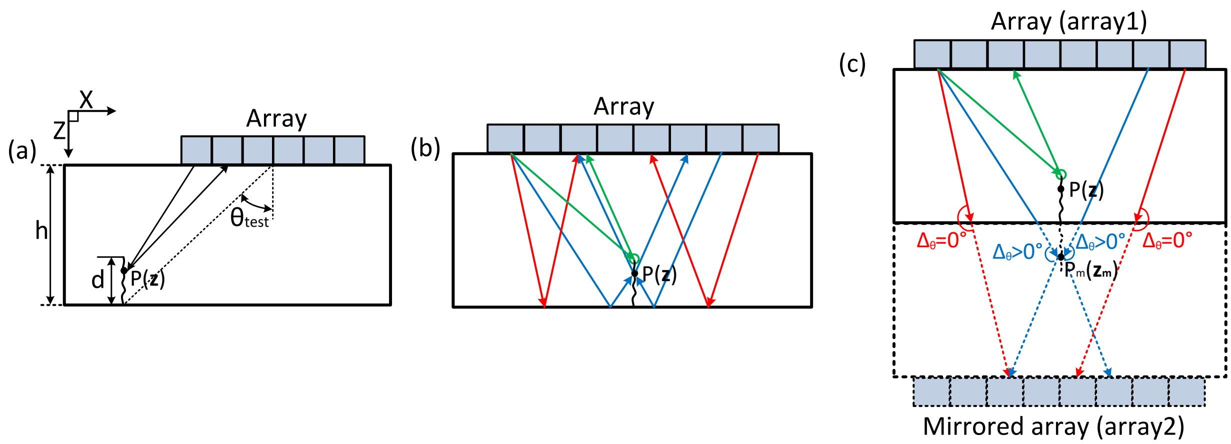

FIG. 2. (a) Schematic showing the inspection of a component containing a surface-breaking crack and an example of the direct ray path considered in TFM, (b) Schematic showing the ray paths of different signal components contained in a typical recorded signal during detection; note that the red ray path represents the backwall reflection, the blue ray path represents the 'half-skip' reflection and the green ray path represents the tip diffraction. (c) The related two array configuration with the crack located in the middle of the material and the equivalent ray paths of the signal components shown in (b). The depth of the crack in (c) is twice the depth of the crack in (b).

from the real array to the imaging point P and then from the point P back to the mirrored array, as shown in Fig. 2(c). It is obvious that the ray path from the point P to the mirrored array is equivalent to the ray path from the mirrored point P_m to the real array. It is noted that the same is true for a pre-defect reflection by reciprocity. Based on this, the indicator function of HSTFM is given by

$$I_{HSTFM}(\boldsymbol{z}) = \int_{\Gamma_i}\int_{\Gamma_i} u^S(\boldsymbol{x_r}, \frac{|\boldsymbol{x_t} - \boldsymbol{z}| + |\boldsymbol{x_r} - \boldsymbol{z_m}|}{c_0}; \boldsymbol{x_t}) ds(\boldsymbol{x_r}) ds(\boldsymbol{x_t}). \tag{10}$$

where Γ_i is the surface where transmitters and receivers are located, $\boldsymbol{x_t} \in \Gamma_i$ is the location of the transmitter, $\boldsymbol{x_r} \in \Gamma_i$ is the location of the receiver and $u^S(\boldsymbol{x_r}, t; \boldsymbol{x_t})$ denotes the time domain scattered data from a transmitter located at $\boldsymbol{x_t}$ to a receiver located at $\boldsymbol{x_r}$.

2. Factorization Method

The Factorization Method (FM) is based on the Linear Sampling Method (LSM), which is the first non-iterative inverse scattering algorithm developed to reconstruct the support of the scatterers. These sampling methods utilise the fact that the scattered field can only be generated at the boundary of the scatterer and can not be produced for a point outside the scatterer, as shown in Fig. 1.

The LSM uses an indicator function based on the far-field operator F to determine whether a point $P(\boldsymbol{z})$ is inside or outside the scatterer. Based on the far-field pattern the scattered field defined in Eq. (8), the far-field operator $F : L^2(\mathbb{S}^2) \to L^2(\mathbb{S})$ is defined as

$$(Fg)(\boldsymbol{\hat{x}}) = \int_{\mathbb{S}^1} U^\infty(\boldsymbol{\hat{x}}, k; \boldsymbol{\theta}) g(\boldsymbol{\theta}) ds(\boldsymbol{\theta}) \tag{11}$$

where g is called the Herglotz density. The Herglotz density corresponds to the density of plane waves in each direction superposed to form an incident field v_g, which is defined as

$$v_g(\boldsymbol{x}) = \int_{\mathbb{S}^1} exp(ik\boldsymbol{x} \cdot \boldsymbol{\hat{x}_0}) g(\boldsymbol{\hat{x}_0}) ds(\boldsymbol{\hat{x}_0}) \tag{12}$$

where $\mathbb{S}^1$ denotes the unit circle in $\mathbb{R}^2$, v_g is also called the Herglotz wavefunction. The far-field pattern of the scattered field created by the incident field v_g is actually equivalent to the Fg in Eq. (11). Here we introduce the far-field pattern of the Green's function (Cakoni and Colton, 2013), namely

$$\Phi_\infty(\hat{\boldsymbol{x}}, k; \boldsymbol{z}) = \frac{exp(i\pi/4)}{\sqrt{8k\pi}} e^{-ik\hat{\boldsymbol{x}}\cdot\boldsymbol{z}} \tag{13}$$

Then, the far-field operator of a sampling point $P(\boldsymbol{z})$, $\boldsymbol{z} \in \Omega$ is defined as

$$Fg_{\boldsymbol{z}} = \Phi_\infty(\hat{\boldsymbol{x}}, k; \boldsymbol{z}) \tag{14}$$

According to (Cakoni and Colton, 2003; Fioralba and David, 2003), the following are true:

- if $\boldsymbol{z} \in D$, then for every $\varepsilon > 0$, there exists a solution $g_{\boldsymbol{z}}^{\varepsilon}$ that

$$||Fg_{\boldsymbol{z}}^{\varepsilon}(\cdot) - \Phi_\infty(\cdot, \boldsymbol{z}, k)||_{L^2(\Omega)} < \varepsilon; \tag{15}$$

  and

$$\lim_{z\to\partial D} ||g_{\boldsymbol{z}}^{\varepsilon}||_{L^2(\Omega)} = \infty, \tag{16}$$

$$\lim_{z\to\partial D} ||v_{g_{\boldsymbol{z}}^{\varepsilon}}||_{H^1(D)} = \infty, \tag{17}$$

  where $v_{g_{\boldsymbol{z}}^{\varepsilon}}$ is the Herglotz wavefunction with density $g_{\boldsymbol{z}}^{\varepsilon}$.

- if $\boldsymbol{z} \in \mathbb{R}^2 \backslash \bar{D}$, then for every $\varepsilon > 0$ and $\delta > 0$, there exists a solution $g_{\boldsymbol{z}}^{\varepsilon}$ that

$$||Fg_{\boldsymbol{z}}^{\varepsilon,\delta}(\cdot) - \Phi_\infty(\cdot, \boldsymbol{z}, k)||_{L^2(\Omega)} < \varepsilon + \delta; \tag{18}$$

  and

$$\lim_{\delta\to 0} ||g_{\boldsymbol{z}}^{\varepsilon,\delta}||_{L^2(\Omega)} = \infty, \tag{19}$$

$$\lim_{\delta\to 0} ||v_{g_{\boldsymbol{z}}^{\varepsilon,\delta}}||_{H^1(D)} = \infty, \tag{20}$$

  where $v_{g_{\boldsymbol{z}}^{\varepsilon,\delta}}$ is the Herglotz wavefunction with density $g_{\boldsymbol{z}}^{\varepsilon,\delta}$.

From the above results, it is clear that the $||g_{\boldsymbol{z}}^{\varepsilon}||_{L^2(\Omega)}$ becomes unbounded as $\boldsymbol{z} \to \partial D$ and is small if $\boldsymbol{z} \not\subset \partial D$. The LSM utilises the behaviour of $||g_{\boldsymbol{z}}^{\varepsilon}||_{L^2(\Omega)}$ to reconstruct the support of the scatterer. However, it will meet convergence issues if the data is noise free (Cakoni and Colton, 2013), which motivated the development of the Factorization Method. The FM replaces the far-field operator F by $(F^*F)^{\frac{1}{4}}$, then Eq. (14) becomes

$$(F^*F)^{\frac{1}{4}} g = \Phi_\infty. \tag{21}$$

Picard's theorem shows that $\boldsymbol{z} \in \mathbb{R}^2$ belongs to D if and only if

$$\sum_{i=1}^{\infty} \frac{1}{|\sigma_i|} |\langle \Phi_\infty(\hat{\boldsymbol{x}}, k; \boldsymbol{z}), \psi_i \rangle_{L^2}|^2 < \infty, \tag{22}$$

where $\{\sigma_i, \psi_i, \hat{\psi}_i\}_1^\infty$ is the singular system of far-field operator F. Eq. (22) is also called Picard's criterion. For the detailed derivation of Picard's criterion, we refer to the classical book about the Factorization Method (Kirsch and Grinberg, 2008). Thus, the indicator function of the FM algorithm is given by

$$I_{FM}(\boldsymbol{z}) = \frac{1}{\displaystyle\sum_{i=1}^{\infty} \frac{1}{|\sigma_i|} |\langle \Phi_\infty(\hat{\boldsymbol{x}}, k; \boldsymbol{z}), \psi_i \rangle_{L^2}|^2}. \tag{23}$$

The intensity of Eq. (23) is large on the boundary of the scatterer and is small outside. Eq. (23) only utilises single frequency data, and as a result, the quality of the reconstruction may not be the best possible if the frequency is poorly chosen (Guo *et al.*, 2016b). In order to overcome this problem, the FM which uses the multi-frequency data defined in Eq. (8) was developed, namely

$$I_{FM}(\boldsymbol{z}) = \sum_{j=1}^{M} \frac{1}{\displaystyle\sum_{i=1}^{\infty} \frac{1}{|\sigma_i|} |\langle \Phi_\infty(\hat{\boldsymbol{x}}, k_j; \boldsymbol{z}), \psi_i \rangle_{L^2}|^2}. \tag{24}$$

where $1 \leq j \leq M$ and M refers to the number of wave numbers used for calculation. It has been proved in (Guzina *et al.*, 2010) that this multi-frequency indicator function is able to avoid some ill-effects that may occur in the single-frequency indicator function when the chosen wavenumber k is close to an interior transmission eigenvalue of the scatterer. The FM used in the following sections of this paper should be understood to be the multi-frequency FM.

3. *Time Domain Sampling Method*

To facilitate the following formulation, we have defined the time-reversed scattered data by

$$u^{tr}(\boldsymbol{x_r}, t; \boldsymbol{x_t}) = \begin{cases} u^S(\boldsymbol{x_r}, T - t; \boldsymbol{x_t}), \quad 0 \leq t \leq T, \\ \\ 0, \quad t < 0, \end{cases} \tag{25}$$

if the time domain scattered data u^S is given, where $\boldsymbol{x_t} \in \Gamma_i$ is the location of the transmitter, $\boldsymbol{x_r} \in \Gamma_i$ is the location of the receiver, Γ_i is the surface where transmitters and receivers are located and $u^S(\boldsymbol{x_r}, t; \boldsymbol{x_t})$ denotes the time domain scattered data from a transmitter located at $\boldsymbol{x_t}$ to a receiver located at $\boldsymbol{x_r}$. Inspired by the frequency domain sampling methods (Ito *et al.*, 2012; Potthast, 2010), Guo et al (Guo *et al.*, 2016a) developed the Time Domain Sampling method as a strengthened TFM. Asssuming the time-reversed scattered data u^{tr} is given, the indicator function of TDSM is given by

$$I_{TDSM}(\boldsymbol{z}) = \int_0^T \int_{\Gamma_i} \left(\int_{\Gamma_i} u^{tr}(\boldsymbol{x_r}, \tau - \frac{|\boldsymbol{z} - \boldsymbol{x_r}|}{c_0}; \boldsymbol{x_t}) ds(\boldsymbol{x_r}) \right)^2 ds(\boldsymbol{x_t}) d\tau. \tag{26}$$

The TDSM shares the same essential requirement of the imaging scheme of the FM, that is to find a spatial varying indicator function which has significant difference in values for points inside and outside the scatterer. In fact, the indicator function of the TDSM (Eq. (26)) is similar to the indicator function of the TFM (Eq. (9)), but the indicator (Eq. (26)) has an integration over the recording time T and a square of the integrand, thus, Guo et al (Guo *et al.*, 2016a) believe that these differences in indicator function will help the TDSM to achieve a better performance over the standard TFM. Although the theory behind the TDSM is only partially resolved, the TDSM has already been implemented for imaging point-like scatterers and regular-size cracks, and achieved satisfactory results on these applications (Guo *et al.*, 2016a).

III. ELIMINATING BACKWALL EFFECTS

A. Imaging setup

In this paper, we consider the problem as shown in Fig. 2(a). There is a component which has two flat parallel surfaces and a thickness of h. A surface-breaking crack with a depth of d appears perpendicular to the backwall. An ultrasonic phased array is placed on the upper surface to detect this surface-breaking crack. We define the angle θ_{test} as the angle between the line joining the centre of the array to the point where the crack intersects the backwall and the vertical line going through the array centre. Thus, based on θ_{test}, the horizontal distance between the array centre and the crack position is $h \times \tan\theta_{test}$.

In fact, the angle θ_{test} not only determines the relative position between the crack and the array, but also relates to the available viewing aperture or the angle of view. In Fig. 3, we compare the aperture difference between two different imaging configurations based on the same array and the same component, one with the crack located directly beneath the array ($\theta_{test} = 0°$), another one with the crack located a distance from the array (usually, $\theta_{test} = 30°$ or $45°$). It is obvious that the biggest aperture can be achieved when $\theta_{test} = 0°$. In some papers, for example (Felice *et al.*, 2014), the array was placed at a distance from the crack ($\theta_{test} = 45°$), so that the backwall reflection can be easily separated from the defect signal. However, this method will not only result in a small viewing angle but also a longer ray path and increasing attenuation. With longer path lengths the coherent noise from grain scattering will be worse, and the signal-to-noise ratio will be reduced for greater attenuation. Also, the (often necessary) introduction of wedges will introduce noise and reduce amplitude further. In order to achieve the biggest aperture and improve the signal strength, the incident angle θ_{test} was set to be zero in this paper.

Assuming a zero incident angle, since the planar backwall is a very strong reflector for the ultrasound, a typical recorded signal during detection will contain three components of primary interest in this paper: the backwall reflection, the ‘half-skip’ reflection and the tip diffraction, as shown in Fig. 2(b). It should be noted that other components can be present, such as a second ‘half-skip’ signal if the receiver is not at the same location as the source, a ‘full-skip’ signal from the defect (likely from tip diffraction), as well as a range of multiply scattered signals (depending on the defect) and multiple components corresponding to mode conversion at the backwall. Among the three components of primary interest, the ‘half-skip’

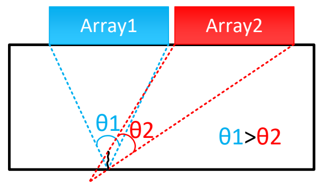

FIG. 3. Schematic showing the aperture difference between two different imaging setups.

reflection and the tip diffraction will be referred to as the defect signal in this paper as they contain information about the defect. The backwall reflection has a much stronger energy than the defect signal as the backwall reflection is the direct specular reflection from the array to the backwall and back to the array, yet provides no information about the defect.

B. Signal overlap problem

In a typical FMC dataset acquired based on the imaging configuration shown in Fig. 2(a) when $\theta_{test} = 0°$, the defect signal and the backwall reflection often overlap in both the time and frequency domains. In order to visually study the overlap of the defect signal and the backwall reflection, we perform a numerical simulation using a finite element model which was created in Abaqus (Dassault Systemes Simulia Corp., Providence, RI) to approximate simulated array data. In keeping with the theoretical analysis in Section II, a 2D FE model is used to analyse this problem under the assumption that all the properties are uniform out of the plane. Here, as the shear wave and the mode conversions between the longitudinal and shear wave always arrive later than the longitudinal wave, making the use of longitudinal waves more logical in practice, only a longitudinal wave was excited and recorded for simplicity (Drozdz, 2008). This is also in keeping with previous work with these

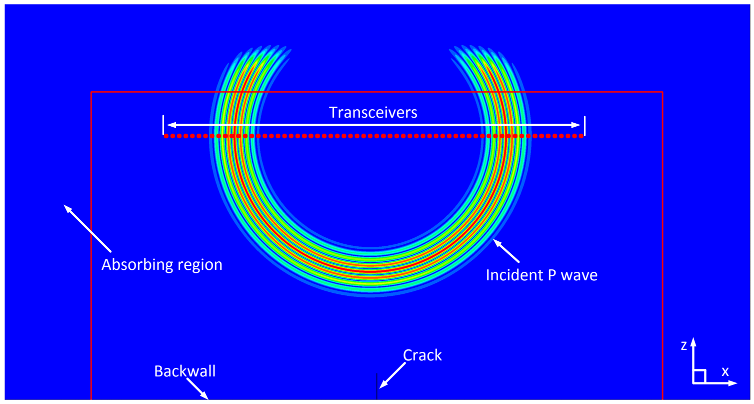

FIG. 4. Snapshot of the FE model used for simulation in Abaqus (Dassault Systemes Simulia Corp., Providence, RI). The length of the crack is 2λ, the thickness of the component is 20λ and the distance between two transceivers of the array is 0.5λ. Frequency is 2MHz, giving a wavelength (λ) of 3mm.

algorithms which have just considered the longitudinal waves (Fan *et al.*, 2014; Felice *et al.*, 2014; Tant *et al.*, 2017). The material used for simulation is isotropic steel with a density of $7700kg/m^3$, a Youngs modulus of $195GPa$ and a Poisson ratio of 0.28. The element used in this model is the linear 2D plane strain element. The phased array has 64 elements and the wave generated by the array is a Hann windowed 5 cycle tone burst with a central frequency 2MHz. Thus, the wavelength λ of the longitudinal wave is about 3mm. To make this model more general, all of the geometric lengths are defined relative to the wavelength. Here, the length of the crack is 2λ, the thickness of the component is 20λ and the distance between two transceivers of the array is 0.5λ. Absorbing layers (Rajagopal *et al.*, 2012) were attached to the model to absorb any wave entering them, acting as 'reflectionless boundaries', to effectively model a small section of an infinite region. Fig. 4 shows a snapshot from the FE model used in Abaqus.

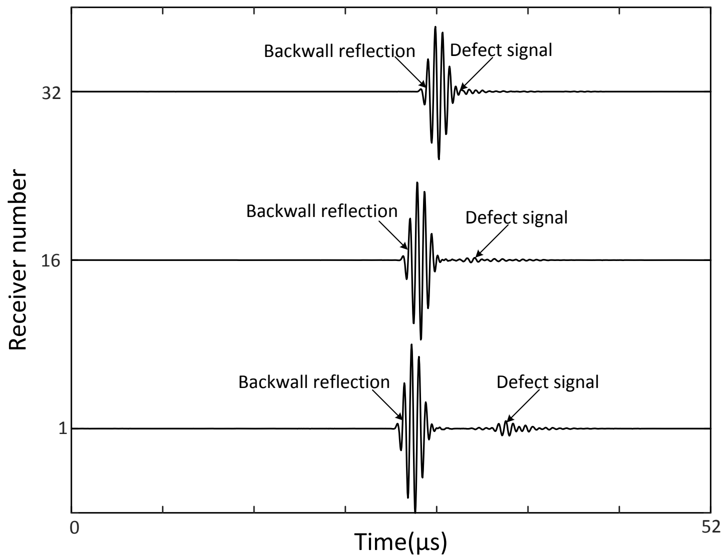

FIG. 5. The time traces of three different elements based on simulated FMC data. Note that element 1 is used as the transmitter while all the elements used as receivers.

From the simulated FMC data from this model, we observed that in the case of detecting the near surface defect, it is easy for the backwall reflection and the defect signal to overlap with each other, and the overlap phenomenon happens in both time and frequency domains (Zhang *et al.*, 2016), as shown in Fig. 5. Additionally, from Fig. 5, we can also see that the amplitude of the backwall reflection is always much stronger than the defect signal. These problems make the extraction of the defect signal challenging.

The overlap phenomenon will also seriously affect the imaging result. Fig. 6 shows the imaging results of TFM, FM and TDSM based on the measured signal containing both the backwall reflection and the defect signal. From Fig. 6, it is clear that in all of the three images, the indication of the crack is masked by the strong indications of the backwall and artefacts introduced by the backwall reflection.

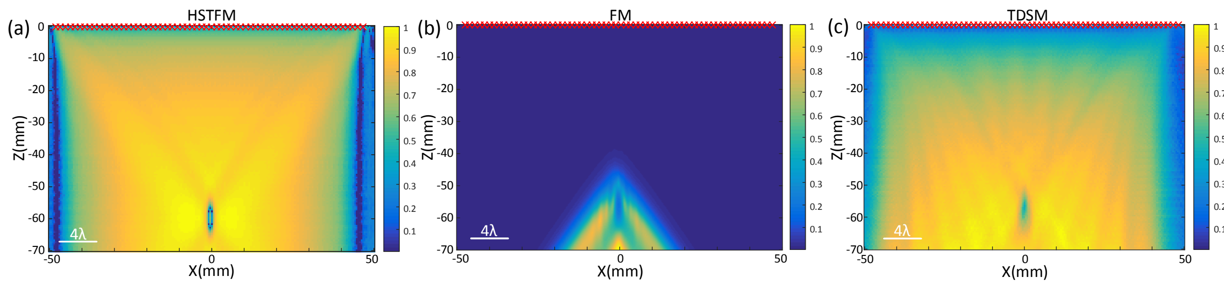

FIG. 6. Results from setup shown in Fig. 4. (a) HSTFM, (b) FM using 10 uniformly distributed frequencies between 1.5MHz and 2.5MHz, and (c) TDSM images based on the overall signal. The red 'X' symbols at the top of the images represent the location of the transceivers and the amplitude is normalized to the maximum value in each image. The results here were from simulated data.

Thus, in order to get a strong and clear indication of the crack through these imaging algorithms, the primary problem for imaging a near surface defect at $\theta_{test} = 0°$ is how to eliminate the effects introduced by the strong backwall reflection. In response, we have developed several methods to eliminate the backwall effects and to ensure a clear and strong indication of the crack, these methods will be described in detail below.

C. Backwall subtraction method

One possible way of extracting the pure defect signal from the overall signal is to measure the backwall reflection of a defect-free copy of the component, then extract the scattered field through a subtraction, a method we will refer to as the baseline subtraction. However, this method is not practical in real inspection as it is not possible to achieve a defect-free copy of the component, so in most of the occasions, the acquired FMC data is the only available data. As a result, FMC subtraction has been developed in (Zhang *et al.*, 2018)

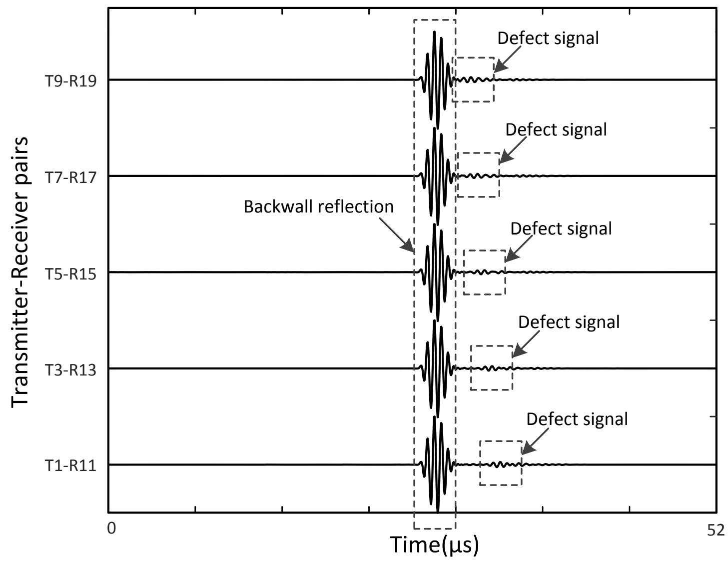

FIG. 7. Several time traces of element pairs of the same lateral separation.

to estimate the the backwall reflection based on the FMC data. This method relies on the phenomenon that for element pairs of the same lateral separation, the length of ray paths of backwall reflections are identical but the ray paths of the defect signals are different for the case of two planar surfaces and homogeneous material. That means these signals will have the same arrival time and amplitude of the backwall reflection but different arrival time and amplitude of the defect signal (Fig. 7).

Based on this, according to (Zhang *et al.*, 2018), if we denote the recorded time trace with the ith element used as transmitter and the jth element used as receiver by $I(i,j)$, the defect signal $S(i,j)$ can be estimated as:

$$S(i,j) = I(i,j) - \frac{1}{2(N-|i-j|)} \sum_{i=1}^{N-|i-j|} \left(I(i, i+|i-j|) + I(i+|i-j|, i)\right), \tag{27}$$

where $i = 1 \cdots N$, $j = 1 \cdots N$ and N is the number of array element. Readers are referred to (Zhang *et al.*, 2018) for a more detailed derivation of the FMC subtraction. In this paper, if not otherwise specified, the summation and averaging in Eq. (27) is implemented over the full time duration. The main disadvantage of the FMC subtraction is that the time traces of the paired outer elements will undergo less averaging; it is acknowledged that this could be more problematic because these components are likely to encode more information on the half-skip for a flat crack-like defect perpendicular to the surface. Because of this, there will always exist some residue of the backwall reflection after subtraction, which may introduce artefacts into the images.

Fig. 8 compares different imaging algorithms based on the signal before and after FMC subtraction. Fig. 8 (a), (b) and (c) are the HSTFM, FM and TDSM results based on the original FMC data, and these three images are the zoomed-in views of the images in Fig. 6. In all of these images, it is clear that the strong indication introduced by the backwall seriously influenced the imaging results. Although the baseline subtraction is impractical in real inspections, it is easy to implement through simulations. In order to provide benchmark results that can support the effectiveness of the FMC subtraction, the imaging results based on the equivalent defect-free model are shown in Fig 8 (d)-(f) and the imaging results based on the data processed by the baseline subtraction are shown in Fig. 8 (g)-(i). Fig. 8 (j), (k) and (l) are the HSTFM, FM and TDSM results based on the FMC data after the FMC subtraction. Obviously, by using the FMC subtraction, there are significant improvements in the imaging results. For the HSTFM and the TDSM (Fig. 8(j) and (l)), the FMC subtraction shows excellent performance as the imaging results after FMC subtraction have very strong and clear indications of the crack and the residue backwall reflections only introduce some uniform background noise which could be eliminated by post-processing the image, such

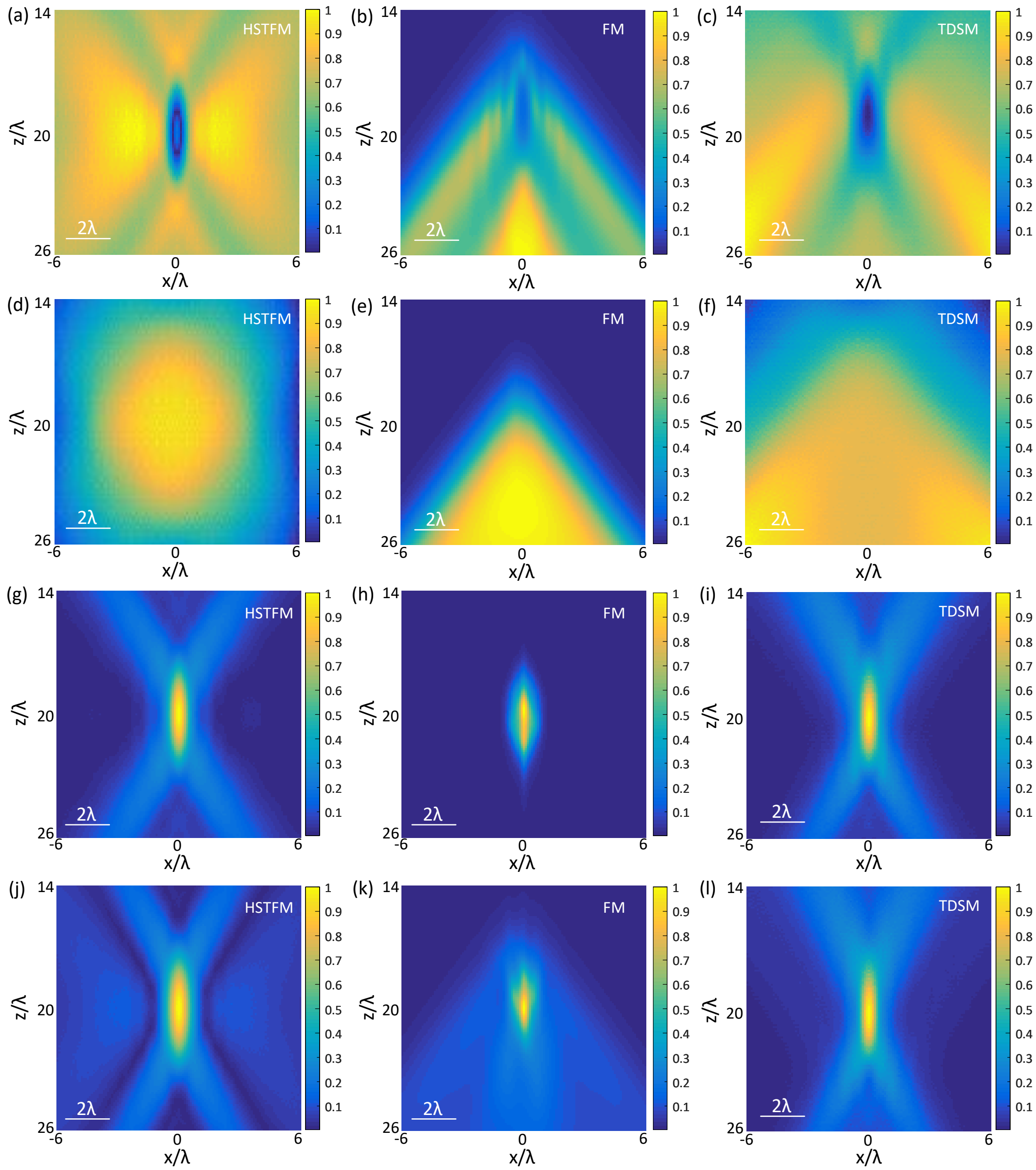

FIG. 8. Results from setup shown in Fig. 4. (a) HSTFM, (b) FM using 10 uniformly distributed frequencies between 1.5MHz and 2.5MHz, and (c) TDSM images, all based on the original signal. (d)-(f) are as (a)-(c) respectively except with the equivalent defect-free model. (g)-(i) are likewise the same algorithms as (a)-(c) except based on the signal after baseline subtraction. (j)-(l) are likewise the same algorithms as (a)-(c) except based on the signal after FMC subtraction. All images have been normalised to the maximum value in each image.

as thresholding to remove artefacts below a certain level – any estimated intensity below a certain level is set to zero (White and Ghosal, 2014). It is acknowledged that this approach is only possible when the artefacts are weak relative to the defect signal. For the FM, the FMC subtraction also helps to achieve a sharp and strong indication of the crack (see Fig. 8(k)), which means the majority of the backwall reflection has been removed. However, as the FM imaging algorithm is more sensitive to noise than the HSTFM and the TDSM, the residual backwall reflection brings more obvious artefacts to the FM image compared to the HSTFM and the TDSM. These artefacts are the 'side bars' near the strong indication of the crack in Fig. 8(k), which may raise the risk of falsely judging the type of the defect. Note that since FMC subtraction is a preprocessing method which operates on the data itself, rather than being incorporated into the algorithm, this method is theoretically suitable for any imaging algorithm which utilises the scattered signal to reconstruct the defect.

D. Weighting function method for HSTFM

Apart for the FMC subtraction, we also developed a specific method for the HSTFM, which is called the weighting function in this paper. The weighting function method is inspired by the work done by P. Huthwaite in (Huthwaite, 2016), where it is shown that the subtraction of the incident wave is unnecessary when imaging using Diffraction Tomography (DT) as the effects introduced by the incident wave will vanish automatically in the DT algorithm. Also, in (Simonetti and Huang, 2008), F. Simonetti et al. have found that there is a linear mapping between Beamforming (BF) and DT. As TFM or HSTFM is actually a BF algorithm, the results in (Huthwaite, 2016) can be directly applied to HSTFM. Since

HSTFM only considers the 'half-skip' ray paths which are reflected on the backwall once, either before or after interacting with the defect, an equivalent ray path of the 'half-skip' ray path can be derived as in Fig. 2(c). Specifically, the equivalent ray paths of the backwall reflection and the 'half-skip' reflection considered in the HSTFM are shown in Fig. 2(c). We neglect the tip diffraction here as the energy of the tip diffraction is too weak compared to the 'half-skip' reflection and backwall reflection. If we define Δ_θ as the angle between the incident direction and the receiving direction in the equivalent model, then all the equivalent ray paths of the backwall reflections will have the same angle $\Delta_\theta = 0°$, as shown in Fig. 2(c). At the same time, from Fig. 2(c), Δ_θ will vary from point to point when considering the 'half-skip' reflection and in this case, Δ_θ cannot be 0° or 180°.

Based on this phenomenon, a weighting function, which can be used as a filter to eliminate the backwall effects, has been introduced as:

$$f(\boldsymbol{x_r}, \boldsymbol{z}; \boldsymbol{x_t}) = |sin(\Delta_\theta)| \tag{28}$$

Readers who are interested in the choice of the weighting function are referred to (Huthwaite, 2016) for more information. It is obvious that the value of this weighting function will tend to 0 if Δ_θ is close to 0° or 180°. Then, this weighting function is integrated in Eq. (10) as:

$$I_{HSTFM}(\boldsymbol{z}) = \int_{\Gamma_i}\int_{\Gamma_i} f(\boldsymbol{x_r}, \boldsymbol{z}; \boldsymbol{x_t}) \cdot u^S(\boldsymbol{x_r}, \frac{|\boldsymbol{y}-\boldsymbol{z}| + |\boldsymbol{x_m}-\boldsymbol{z}|}{c_0}; \boldsymbol{x_t}) ds(\boldsymbol{x_r}) ds(\boldsymbol{x_t}). \tag{29}$$

where Γ_i is the surface where transmitters and receivers are located, $\boldsymbol{x_t} \in \Gamma_i$ is the location of the transmitter, $\boldsymbol{x_r} \in \Gamma_i$ is the location of the receiver and $u^S(\boldsymbol{x_r}, t; \boldsymbol{x_t})$ denotes the time domain scattered data from a transmitter located at $\boldsymbol{x_t}$ to a receiver located at $\boldsymbol{x_r}$. Fig. 9(a) and Fig. 9(c) are the HSTFM images based on the original FMC data without and

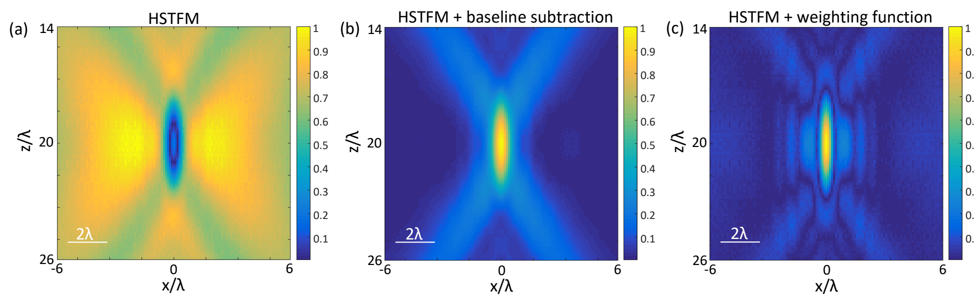

FIG. 9. Results from setup shown in Fig. 4. (a) Conventional HSTFM image based on the overall signal, (b) Conventional HSTFM based on the data proposed by the base line subtraction, (c) Conventional HSTFM with the weighting function image based on the overall signal. The images were normalized to the maximum value in each image. The results here were from simulated data.

with the weighting function, respectively. Again, the imaging results based on the baseline subtraction are shown in Fig. 9(b) to support the effectiveness of the weighting function method.

From Fig. 9, it is obvious that by using the conventional HSTFM together with the weighting function, the effects introduced by the backwall reflection vanish automatically, which means the weighting function shows an excellent ability to eliminate the backwall effects. As a result, a good indication of the crack can be imaged without the backwall subtraction when using the HSTFM with the weighting function. Using the weighting function to eliminate the backwall effects will be called the 'weighting function method' throughout this paper.

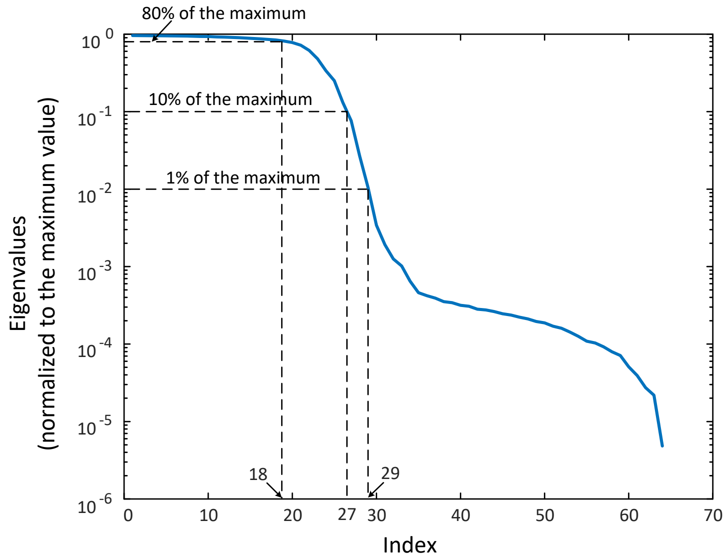

FIG. 10. Singular values spectrum for the simulated FMC data at 2MHz.

E. Truncation method for FM

If we observe the indicator function of the FM algorithm (Eq. (23) or Eq. (24)), it can be found that the calculation of the FM image heavily depends on the singular values and the corresponding eigenvectors of the far-field operator. It has been proved that the singular values and the relevant eigenvectors of the far-field operator are linked to the scatterers (Prada and Fink, 1994), which means by using different singular values, the FM is able to reconstruct different scatterers. Based on this theory, an imaging experiment has been conducted using different numbers of singular values for the calculation. In these cases, a threshold criterion can be used to determine how many singular values will be used for imaging.

As shown in Fig. 10, 10% of the maximum means that the calculation of the FM algorithm will only use the singular values whose amplitudes are bigger than 10% of the maximum

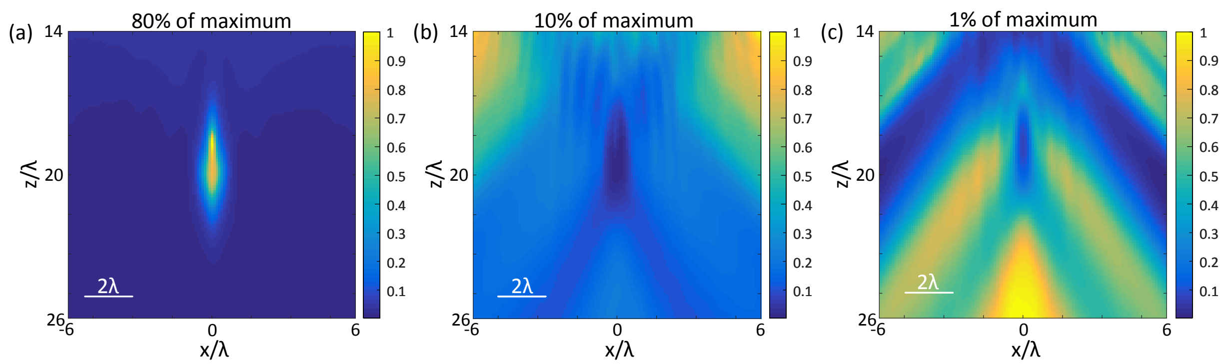

FIG. 11. Results from setup shown in Fig. 4. (a) FM image using the 80% criterion, (b) FM image using the 10% criterion, (c) FM image using the 1% criterion. The FM uses 10 uniformly distributed frequencies between 1.5MHz and 2.5MHz in each image. The images were normalized to the maximum value in each image. The results here are from simulated data.

value at each frequency. Three threshold values have been set, 80%, 10% and 1%, and the imaging results of the FM algorithm based on these 3 criteria are shown in Fig 11.

From Fig. 11(a), it is clear that the image only contains a strong indication of the crack, and there are no artefacts introduced by the backwall reflection near the indication of the crack. By using more singular values (10% of maximum), the backwall effects start to dominate the image, see Fig. 11(b). If most of the singular values are used (1% of maximum), the indication of the crack is totally masked by the backwall effects, see Fig. 11(c). From these images, it indicates that the most significant singular values (80% of the maximum) are linked to the crack and the information brought by the backwall reflections are encoded in the smaller singular values. Here, based on the imaging results, a criterion of 80% of the maximum value at each frequency was found to be a good threshold for the FM algorithm to eliminate the backwall effects, indicating that the backwall reflection is not included in the FM image when the small singular values are truncated. As this method contains a truncation of the small singular values, this method is called the 'truncation method' throughout this paper. Note that the threshold criterion depends on the type of defect and the structure of the component, so the threshold criterion should be tuned for different inspection scenarios.

One problem of this method is that by ignoring the the small singular values, it leads to a loss of information. In the case of limited-view imaging, a common way to compensate for the loss of information is to increase the available aperture (Hutt and Simonetti, 2010b). In (Hutt and Simonetti, 2010a), with the purpose of achieving a more detailed image in the case of limited-view, T. D. Hutt has developed a method which utilises the backwall to provide additional views. This method essentially increases the available aperture for a specific array, however, this method is not able to provide good results if the defect is located close to the backwall. Inspired by this, a new method has been developed to increase the available aperture in the case of imaging the near backwall defects, especially the surface-breaking cracks. Based on the derivations of the HSTFM and the weighting function for the HSTFM, it is obvious that the two models in Fig. 2(b) and (c) are related.

Here, we are now focusing on the relationship between the defect signal (tip diffraction and 'half-skip' reflection) shown in Fig. 2(b) and its equivalent wave shown in Fig. 2(c). In order to facilitate the following derivations, the backwall reflection and its equivalent wave in Fig. 2(b) and (c) are not considered. For the model shown in Fig. 2(b), we define the tip diffraction as U_t^∞, the 'half-skip' reflection as U_h^∞ and the overall defect signal as U^∞, while for the model shown in Fig. 2(c), we define the forward scattering from array1 to array2 as U_{12}^{∞}, the forward scattering from array2 to array1 as U_{21}^{∞}, the backward scattering from array1 back to array1 as U_{11}^{∞} and the backward scattering from array2 back to array2 as U_{22}^{∞}. The ray path of the tip diffraction based on the model shown in Fig. 2(b) is actually equivalent to the ray path of the backward scattering from array1 back to array1 based on the model shown in Fig. 2(c), similarly, the ray path of the 'half-skip' reflection based on the model shown in Fig. 2(b) is actually equivalent to the ray path of the forward scattering from array1 to array2 based on the model shown in Fig. 2(c). Because of the symmetry of the model shown in Fig. 2(c) and the principle of reciprocity, it is clear that $U_{11}^{\infty} = U_{22}^{\infty}$ and $U_{12}^{\infty} = U_{21}^{\infty}$. Based on all these facts, we have

$$U^{\infty} = U_t^{\infty} + U_h^{\infty}, \tag{30}$$

$$U_t^{\infty} = U_{11}^{\infty} = U_{22}^{\infty}, \tag{31}$$

$$U_h^{\infty} = U_{12}^{\infty} = U_{21}^{\infty}. \tag{32}$$

This makes the assumption that the singular value filtering approach developed for the standard FM, which effectively attempts to include just the tip-diffraction signals in the reconstruction, is also valid for the 'half-skip' components, where the waves interacting with the defect have reflected once off the backwall. As the energy of the 'half-skip' reflection and the energy of the specular reflection are much larger than the energy of the tip diffraction, it is clear that

$$U_h^{\infty} \gg U_t^{\infty}, \quad U_t^{\infty} \approx 0, \tag{33}$$

$$U_{12}^{\infty} \gg U_{11}^{\infty}, \quad U_{11}^{\infty} \approx 0. \tag{34}$$

Then, Eq. (30) becomes

$$U^{\infty} \approx U_{12}^{\infty}, \quad U_{12}^{\infty} = U_{21}^{\infty} = U_{h}^{\infty}. \tag{35}$$

Thus, the full data-set U_{full}^{∞} which can be recorded based on the model shown in Fig. 2(c) becomes

$$\begin{aligned} U_{full}^{\infty} &= \begin{pmatrix} U_{11}^{\infty} & U_{12}^{\infty} \\ U_{21}^{\infty} & U_{22}^{\infty} \end{pmatrix} \\ &\approx \begin{pmatrix} 0 & U^{\infty} \\ U^{\infty} & 0 \end{pmatrix} \end{aligned} \tag{36}$$

Through Eq. (36), we can reconstruct the full data-set U_{full}^{∞} based on the model shown in Fig. 2(c) through the defect signal recorded in the model shown in Fig. 2(b). As a result, the available imaging aperture is essentially increased by using the reconstructed U_{full}^{∞} and the relevant imaging configuration (Fig. 2(c)) for the FM algorithm. This method is called the mirror enhancement throughout this paper and is used to compensate for some of the lost information when the truncation method is used with the FM algorithm to eliminate the backwall effects for near backwall defects. It should be noted that T. Hutt et al. (Hutt and Simonetti, 2010a,b) have developed a method that uses a modified Green's function in the calculation of the FM image to utilise the effect of mirror, however, their method has shown a poor performance for near backwall defects.

The effect of the mirror enhancement is shown in Fig. 12. From this, it is clear that by using the FM algorithm together with the truncation method and the mirror enhancement,

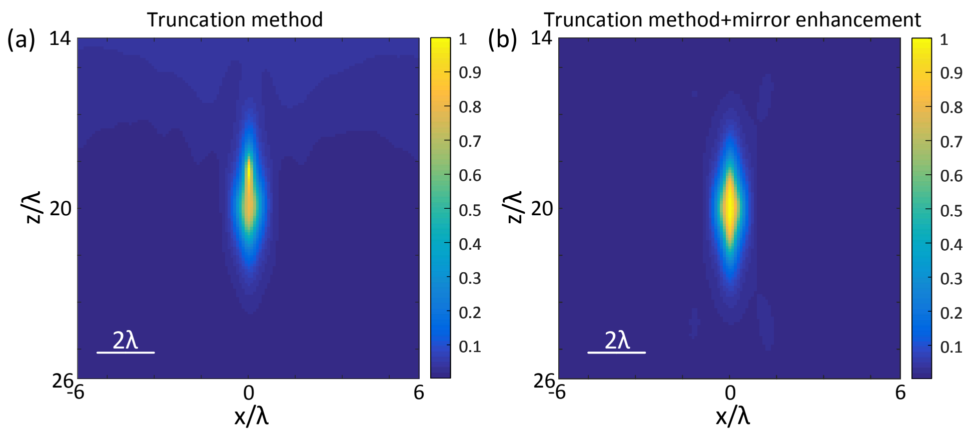

FIG. 12. Results from setup shown in Fig. 4. (a) FM image using the the truncation method to eliminate the backwall effects, (b) FM image using the the truncation method to eliminate the backwall effects and the mirror enhancement to improve the image quality. The FM uses 10 uniformly distributed frequencies between 1.5MHz and 2.5MHz in each image and the images were normalized to the maximum value in each image. The results here were from simulated data.

the majority of the backwall effects can be removed without causing an obvious image degradation.

IV. EXPERIMENTAL VALIDATION

For experimental validation, an array with the parameters shown in Table I was used for the experimental measurements. This array probe was manufactured by IMASONIC ($Haute - Saône$, France). The sample used for the experimental measurements was a block of $180 \times 450 \times 40$mm, 304 stainless steel. This sample contains a surface-breaking crack with a size (depth $\times$ length) of 5×20.4 mm and an average opening of $73.0\mu m$, see Fig. 13. The crack was produced by using controlled thermal fatigue loading (Kemppainen *et al.*, 2003).

TABLE I. Specification of the array transducer used in experimental measurements.

Element number	Central frequency	Bandwidth	Element width	Element pitch	Aperture size
	(MHz)	(-6dB; MHz)	(mm)	(mm)	(mm)
48	2.5	1.66 to 3.22	1.0	1.2	57.4

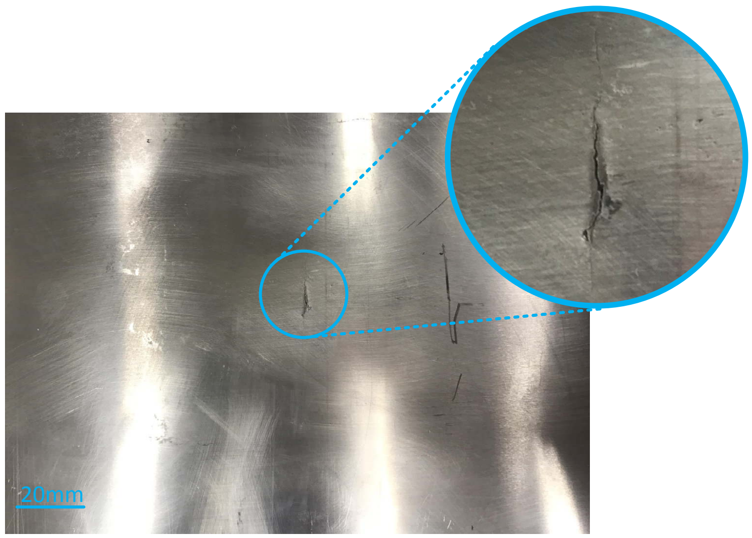

FIG. 13. The picture of the sample and the crack opening.

The depth of the crack is estimated empirically, by destructively analysing previous samples made under the same loading conditions, while the length and opening are measured from the micrograph (Virkkunen *et al.*, 2009). The surfaces of this sample are flat and smooth. The flawed sample was produced and measured by Trueflaw Ltd. The longitudinal wave speed in 304 stainless steel is $5920m/s$, thus, the depth of the crack is about 2λ for the centre frequency of the 2.5MHz probe. The FMC data were collected from this sample using the 2.5MHz probe, with the same array configuration of $\theta_{test} = 0$ (Fig. 3(a)).

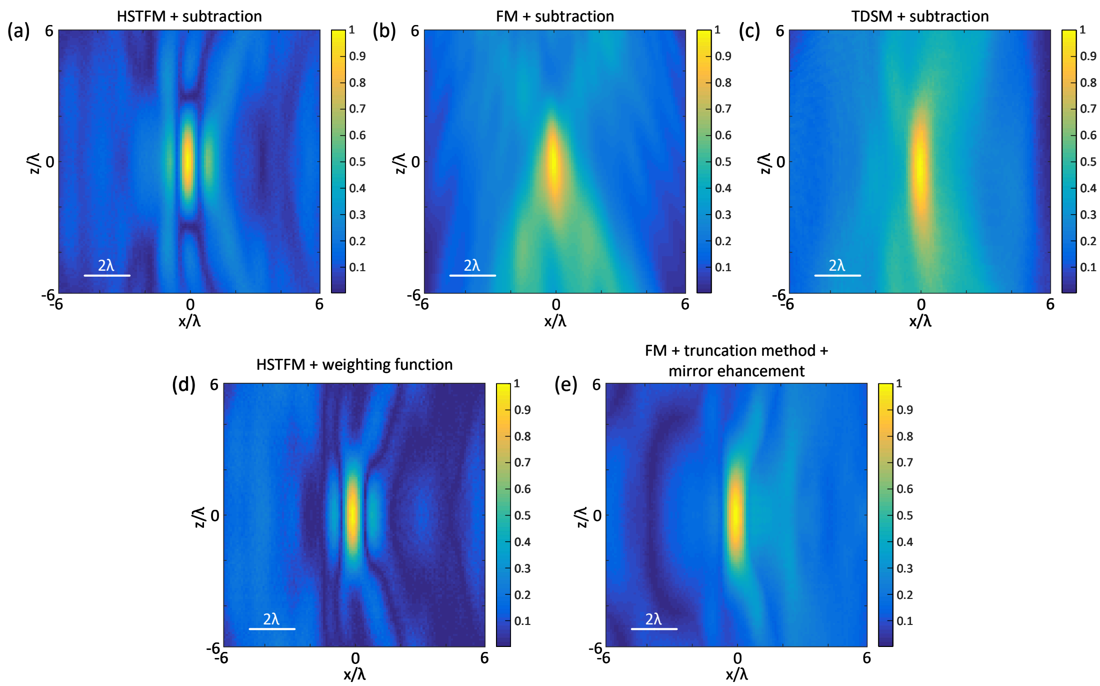

FIG. 14. (a) HSTFM, (b) FM, and (c) TDSM images based on the FMC data after FMC subtraction, (d) HSTFM with the weighting function image based on the original FMC data, (e) FM with the truncation method and the mirror enhancement image based on the original FMC data. The FM uses 10 uniformly distributed frequencies between 2.5MHz and 3MHz in each image and the images were normalized to the maximum value in each image. The results here were from experimental data.

After the acquisition of the FMC data, the three imaging algorithms, i.e. the HSTFM, the FM and the TDSM, together with the relevant methods developed to eliminate the backwall effects, were applied to the same FMC data, and all the imaging results are shown in Fig. 14. These image results based on the experimental data show a good consistency with those obtained from simulated data.

All the images in Fig. 14 show a very good indication of the surface-breaking crack, indicating that the methods developed in this paper, i.e. the FMC subtraction, the weighting function for the HSTFM, and the truncation method for the FM, can successfully eliminate the backwall effects while imaging the near backwall defects, although it is recognised that this is an idealised lab-based setup. The difference between the FMC subtraction and the weighting function method (or the truncation method) is that the FMC subtraction attempts to remove the backwall reflection in the FMC data while the weighting function method (or the truncation method) attempts to directly remove the backwall effects in the imaging process. From the imaging results, it is clear that the images processed by the direct methods (the weighting function method and the truncation method) show a better image quality and contain fewer artefacts than the images processed by the FMC subtraction, see Fig. 14(a) vs Fig. 14(d) (or Fig. 14(b) vs Fig. 14(e)). This is because the FMC subtraction will leave a residual backwall reflection in the FMC data after subtraction. The advantage of the FMC subtraction is that this method is very easy to implement as no prior knowledge is needed and it is therefore suitable for any imaging algorithm which utilises the scattered signal to reconstruct the defect. Unlike the FMC subtraction, the weighting function method is developed specifically for HSTFM while the truncation method for the FM requires tuning of the threshold criterion for different imaging configurations. The imaging results also indicate that the three imaging algorithms, i.e. the HSTFM, the FM and the TDSM, have the potential to reconstruct small near backwall defects if the backwall effects can be removed.

V. CONCLUSIONS

In this paper, new techniques to image near-surface defects and to eliminate the backwall effects were presented. This involves both the imaging algorithms themselves and pre-processing methods to eliminate the backwall effects. Three imaging algorithms, the HSTFM, the FM and the TDSM, were chosen in this paper to solve the problem of imaging the near backwall defects. However, the three imaging algorithms failed to image the near backwall defects when applied to the original FMC data which contains the backwall reflection, because this will introduce strong artefacts to the images. In response to this problem, three methods were explored in this paper to eliminate the backwall effects and to ensure a good image quality of the defect. FMC subtraction attempts to reconstruct the pure backwall reflection based on the original FMC data and the defect signal can be simply extracted by subtraction. The implementation of this method needs no prior knowledge of the component geometry and this method is theoretically suitable for any imaging algorithms, although it does require the backwall to be parallel to the array. This method will leave some residual backwall reflection in the data, but this is not entirely problematic as the majority of the backwall reflection will be removed. The second method, the weighting function method, is based on the angle difference between the backwall reflection and the defect signal considered in the HSTFM. The weighting function method is developed specifically for HSTFM and can directly filter the artefacts introduced by the backwall reflection in the HSTFM image. The third method, the truncation method, attempts to control the behaviour of the image by selecting the singular values used for the FM algorithm. The implementation of this method needs to tune the threshold criterion at first. The threshold criterion is used to determine which singular values should be used for calculation and this criterion depends on the geometry of the component and the type of defect expected. The truncation of the singular values will cause a loss of information which may degrade the image quality. To compensate for the loss of information caused by the truncation method, a method called the mirror enhancement has been developed to increase the available aperture when imaging the near backwall defects.

All three imaging algorithms together with the relevant methods to eliminate the backwall effects are tested with simulated and experimental data, and their performance is assessed through the imaging results. Based on the imaging results, it can be concluded that all the methods developed in this paper have shown effectiveness to eliminate the backwall effects and are simple in their implementation at the same time. All the imaging results have shown a significant reduction in artefacts when the described methods were applied. The results also indicate that the three imaging algorithms, i.e. the HSTFM, the FM and the TDSM, are able to image the near backwall defects if the backwall effects are eliminated.

ACKNOWLEDGMENTS

The authors acknowledge UK Research Centre for NDE and EPSRC (Grant No. EP/M016315/1) for funding this work. P. Huthwaite is funded by an EPSRC Early Career Fellowship, grant number EP/M020207/1. The authors would like to thank industrial partners from Wood plc. and Rolls-Royce Submarines for their essential technical assistance.

Bai, L., Velichko, A., and Drinkwater, B. W. (**2015**). “Ultrasonic characterization of crack-like defects using scattering matrix similarity metrics,” IEEE Transactions on Ultrasonics, Ferroelectrics, and Frequency Control **62**(3), 545–559, doi: 10.1109/TUFFC.2014.006848.

Cakoni, F., and Colton, D. (**2003**). “The linear sampling method for cracks,” Inverse problems **19**(2), 279.

Cakoni, F., and Colton, D. (**2013**). Applied Mathematical Sciences *A Qualitative Approach to Inverse Scattering Theory* (Springer US), pp. 62-85.

Chen, B., Ma, F., and Guo, Y. (**2017**). “Time domain scattering and inverse scattering problems in a locally perturbed half-plane,” Applicable Analysis **96**(8), 1303–1325, doi: 10.1080/00036811.2016.1188288.

Cicero, T., Cawley, P., Simonetti, F., and Rokhlin, S. (**2009**). “Potential and limitations of a deconvolution approach for guided wave structural health monitoring,” Structural Health Monitoring **8**(5), 381–395, doi: 10.1177/1475921709102086.

Collins, J. (**1993**). Wiley-Interscience publication *Failure of Materials in Mechanical Design: Analysis, Prediction, Prevention* (Wiley), pp. 374–459.

Colton, D., and Kress, R. (**2013**). *Integral Equation Methods in Scattering Theory* (Society for Industrial and Applied Mathematics, Philadelphia, PA), pp. 66–109.

Drozdz, M. (**2008**). *Efficient Finite Element Modelling of Ultrasound Waves in Elastic Media* (University of London, UK), pp. 90–145.

Fan, C., Caleap, M., Pan, M., and Drinkwater, B. W. (**2014**). “A comparison between ultrasonic array beamforming and super resolution imaging algorithms for non-destructive evaluation," Ultrasonics **54**(7), 1842 – 1850, doi: 10.1016/j.ultras.2013.12.012.

Felice, M. V., Velichko, A., and Wilcox, P. D. (**2014**). "Accurate depth measurement of small surface-breaking cracks using an ultrasonic array post-processing technique," NDT & E International **68**, 105–112, doi: 10.1016/j.ndteint.2014.08.004.

Felice, M. V., Velichko, A., Wilcox, P. D., and Lane, C. J. L. (**2015**). "Depth measurement of small surface-breaking cracks using the half-skip total focusing method," AIP Conference Proceedings **1650**(1), 994–1000, doi: 10.1063/1.4914706.

Fioralba, C., and David, C. (**2003**). "On the mathematical basis of the linear sampling method," Georgian Mathematical Journal **10**(3), 411–425, doi: 10.1515/GMJ.2003.411.

Graham, I., Langer, U., Melenk, J., and Sini, M. (**2013**). Radon series on computational and applied mathematics *Direct and Inverse Problems in Wave Propagation and Applications* (Walter de Gruyter GmbH), pp. 90–145.

Griesmaier, R. (**2011**). "Multi-frequency orthogonality sampling for inverse obstacle scattering problems," Inverse Problems **27**(8), 085005.

Gruber, F. K., Marengo, E. A., and Devaney, A. J. (**2004**). "Time-reversal imaging with multiple signal classification considering multiple scattering between the targets," The Journal of the Acoustical Society of America **115**(6), 3042–3047, doi: 10.1121/1.1738451.

Guo, Y., Hömberg, D., Hu, G., Li, J., and Liu, H. (**2016**a). "A time domain sampling method for inverse acoustic scattering problems," Journal of Computational Physics **314**, 647 – 660, doi: 10.1016/j.jcp.2016.03.046.

Guo, Y., Monk, P., and Colton, D. (**2016**b). "The linear sampling method for sparse small aperture data," Applicable Analysis **95**(8), 1599–1615, doi: 10.1080/00036811.2015.

1065317.

Guzina, B. B., Cakoni, F., and Bellis, C. (**2010**). "On the multi-frequency obstacle reconstruction via the linear sampling method," Inverse Problems **26**(12), 125005.

Holmes, C., Drinkwater, B. W., and Wilcox, P. D. (**2005**). "Post-processing of the full matrix of ultrasonic transmitreceive array data for non-destructive evaluation," NDT & E International **38**(8), 701–711, doi: 10.1016/j.ndteint.2005.04.002.

Huthwaite, P. (**2016**). "Eliminating incident subtraction in diffraction tomography," Proceedings of the Royal Society of London A: Mathematical, Physical and Engineering Sciences **472**(2195), doi: 10.1098/rspa.2016.0707.

Hutt, T., and Simonetti, F. (**2010**a). "Reconstructing the shape of an object from its mirror image," Journal of Applied Physics **108**(6), 064909, doi: 10.1063/1.3468669.

Hutt, T. D., and Simonetti, F. (**2010**b). "Reconstructing the back of a defect from its mirror image," AIP Conference Proceedings **1211**(1), 742–749, doi: 10.1063/1.3362469.

Iakovleva, E., Chatillon, S., Bredif, P., and Mahaut, S. (**2014**). "Multi-mode tfm imaging with artifacts filtering using civa ut forwards models," AIP Conference Proceedings **1581**(1), 72–79, doi: 10.1063/1.4864804.

Ito, K., Jin, B., and Zou, J. (**2012**). "A direct sampling method to an inverse medium scattering problem," Inverse Problems **28**(2), 025003.

Kemppainen, M., Virkkunen, I., Pitkänen, J., Paussu, R., and Hänninen, H. (**2003**). "Advanced flaw production method for in-service inspection qualification mock-ups," Nuclear Engineering and Design **224**(1), 105 – 117, doi: https://doi.org/10.1016/S0029-5493(03)00078-5.

Kinsler, L. E., Frey, A. R., Coppens, A. B., and Sanders, J. V. (**2000**). *Fundamentals of acoustics*, **1** (Wiley), pp. 91–107.

Kirsch, A. (**1996**). Applied Mathematical Sciences *An Introduction to the Mathematical Theory of Inverse Problems* (Springer New York), pp. 173–213.

Kirsch, A., and Grinberg, N. (**2008**). Oxford Lecture Series in Mathe *The Factorization Method for Inverse Problems* (OUP Oxford), pp. 1–35.

Pike, E., and Sabatier, P. (**2002**). Scattering: Scattering and Inverse Scattering in Pure and Applied Science *Scattering: Scattering and Inverse Scattering in Pure and Applied Science* (Acad. Press), pp. 95–175.

Martin-Arguedas, C. J., Romero-Laorden, D., Martinez-Graullera, O., Perez-Lopez, M., and Gomez-Ullate, L. (**2012**). "An ultrasonic imaging system based on a new saft approach and a gpu beamformer," IEEE Transactions on Ultrasonics, Ferroelectrics, and Frequency Control **59**(7), 1402–1412, doi: 10.1109/TUFFC.2012.2341.

Portzgen, N., Gisolf, D., and Blacquiere, G. (**2007**). "Inverse wave field extrapolation: a different ndi approach to imaging defects," IEEE Transactions on Ultrasonics, Ferroelectrics, and Frequency Control **54**(1), 118–127, doi: 10.1109/TUFFC.2007.217.

Potthast, R. (**2010**). "A study on orthogonality sampling," Inverse Problems **26**(7), 074015.

Prada, C., and Fink, M. (**1994**). "Eigenmodes of the time reversal operator: A solution to selective focusing in multiple-target media," Wave Motion **20**(2), 151 – 163, doi: 10.1016/0165-2125(94)90039-6.

Rajagopal, P., Drozdz, M., Skelton, E. A., Lowe, M. J., and Craster, R. V. (**2012**). "On the use of absorbing layers to simulate the propagation of elastic waves in unbounded isotropic media using commercially available finite element packages," NDT & E International **51**, 30–40, doi: 10.1016/j.ndteint.2012.04.001.

Simonetti, F. (**2006**). "Localization of pointlike scatterers in solids with subwavelength resolution," Applied Physics Letters **89**(9), 094105, doi: 10.1063/1.2338888.

Simonetti, F., and Huang, L. (**2008**). "From beamforming to diffraction tomography," Journal of Applied Physics **103**(10), 103110, doi: 10.1063/1.2927433.

Virkkunen, I., Kempainen, M., Ostermeyer, H., Paussu, R., and Dunhill, T. (**2009**). "Grown cracks for ndt development and qualification," Insight - Non-Destructive Testing and Condition Monitoring **51**(5), 271–278, doi: doi:10.1784/insi.2009.51.5.271.

Zhang, C., Huthwaite, P., and Lowe, M. (**2018**). "The application of the factorization method to the subsurface imaging of surface-breaking cracks," IEEE Transactions on Ultrasonics, Ferroelectrics, and Frequency Control **65**(3), 497–512, doi: 10.1109/TUFFC.2018.2793267.

Zhang, J., Drinkwater, B. W., and Wilcox, P. D. (**2010**). "The use of ultrasonic arrays to characterize crack-like defects," Journal of Nondestructive Evaluation **29**(4), 222–232, doi: 10.1007/s10921-010-0080-6.

Zhang, J., Yu, P., and Gang, T. (**2016**). "Measurement of the ultrasonic scattering matrices of near-surface defects using ultrasonic arrays," Nondestructive Testing and Evaluation **31**(4), 303–318, doi: 10.1080/10589759.2015.1093626.

Tant, K. M. M., Mulholland, A. J., and Gachagan, A. (**2017**). "Application of the factorisation method to limited aperture ultrasonic phased array data," Acta Acustica united with Acustica **103**(6), 954–966, doi: doi:10.3813/AAA.919125.

White, J. T., and Ghosal, S. (**2014**). “Multiple testing approaches for removing background noise from images,” in *Topics in Nonparametric Statistics* (Springer), pp. 95–104.